

# Peridynamic analysis for failure modes of concrete gravity dam subjected to underwater blast load

Liwei Wu<sup>1</sup>, Han Wang<sup>2</sup>, Dan Huang<sup>1,\*</sup>

1. College of Mechanics and Materials, Hohai University, Nanjing, 211100, China.

2. Xi'an Research Institution of High Technology, Xi'an, 710025, China.

**Abstract:** A better understanding on failure characteristics of the concrete gravity dam, when subjected to underwater blast load, is significant and crucial for the operation evaluation and protection of dams. In this paper, a peridynamic modeling and numerical analysis for the underwater explosion failure of the concrete gravity dam is presented. The meso-structural characteristics of concrete are taken into account through a modified intermediately homogenized peridynamic (IH-PD) model, where the mechanical behavior of wet concrete is considered as well. The blast-induced failure of concrete is investigated through two benchmark examples, and the validation is established by comparing the available numerical results with corresponding experimental observations. Furthermore, the explosion response and failure mode of the concrete gravity dam subjected to underwater blast load are numerically simulated, and the effects of explosion equivalent, standoff distance, and detonation depth on the gravity dam are analyzed and discussed respectively. The results could be meaningful in the evaluation of safe operation and protection design for the concrete gravity dam.

Keywords: Concrete gravity dam, Underwater blast load, Explosion failure mode, Peridynamics

---

\* Corresponding Author: Dan Huang. Email: [danhuang@hhu.edu.cn](mailto:danhuang@hhu.edu.cn)

## 1. Introduction

During the normal operation of concrete gravity dams, they are likely to suffer from dynamic loading conditions, in terms of wind load, earthquake load, high-velocity impact load, blast load, etc. Moreover, with the rapid development of worldwide advanced weapons, large dams are more likely to be the attacked target. As an unconventional event due to the blast load, once the sudden explosion happens, there will cause extremely serious consequences, which would threaten the lives and property of people. To improve the stability and safety of dams, it is of great significance to study the damage mechanism and failure mode of dams when subjected to blast load.

The experimental test is the most direct method to study the structural response under blast load. Nevertheless, it is so costly and time-consuming that performs experimental tests to analyze the damage and failure of concrete gravity dams to blast load. Recently, with the development of computer technology and computational mechanics, numerical simulation has been the primary approach to investigating the dynamic responses and explosion failure of concrete gravity dams. Much general numerical software has been developed, including LS-DYNA, AUTODYN, ABAQUS/CEL, Air3D, etc. Due to their powerful function and simple operation, they are favored by numerous scholars around the world. Wang et al. [1] proposed a fluid-solid coupling model in LS-DYNA to simulate the interaction between the blast wave propagation and dam structures. The dynamic failure characteristics of concrete gravity dams, when subjected to penetration and explosion, are investigated by Shu et al. [2] through the explicit hydro-code AUTODYN. Zhu et al. [3] developed the fully-coupled (LS-DYNA) and semi-coupled model (ABAQUS/CEL) for the explosion failure analysis of concrete gravity dams under underwater blast load.

For the numerical analysis of the dynamic response of concrete structures, the most

widely used numerical method is the finite element method (FEM) [4], which has strong universality and applicability. Besides, meshless methods have greater geometric flexibility than FEM and own their unique advantages in dealing with complex dynamic problems. At present, the common meshless methods include the discrete element method (DEM) [5], smoothed particle hydrodynamics (SPH) [6] method, reproducing kernel particle method (RKPM) [7], element-free galerkin (EFG) method [8], material point method (MPM) [9], etc. Nevertheless, the aforementioned numerical methods are based on the classical continuum mechanics theory, where the continuity hypothesis is contradictory to reality. It is difficult to break through the limitation in calculation accuracy and efficiency, caused by the local discontinuity and crack tip singularity.

Peridynamics (PD) [10,11], a non-local theory, was presented as a reformulation of the classical continuum mechanics theory. Its main idea, adopting the spatial integral equation instead of the differential equation, makes such a model much more advantageous than other methods when handling discontinuities. Meanwhile, a new description of the damage defined in peridynamics [12], means that cracks could propagate spontaneously without any extra remedies. By means of its advantages for discontinuities, peridynamics has been widely used in the numerical analysis of quasi-static and dynamic fracture in various materials [13–16], impact failure [17–19], fatigue and corrosion modeling [20–23], multi-physical field coupling [24–26] and multi-scale mechanical problems[27–29], etc.

Up to now, peridynamics is hardly used for the explosion problems, but it can still be regarded as a potential method to analyze the damage and failure to blast load. Based on a new peridynamic model combined with the Johnson-Holmquist (JH2) constitutive model, Zhu et al. [30] studied the failure characteristics of rock under blast load. Diyaroglu et al. [31] proved the applicability of peridynamic model to accurately

simulate the nonlinear deformation and damage of composite materials subjected to blast load. Zhang et al. [32] proposed a peridynamic model to analyze the crack propagation in rocks under liquid carbon dioxide explosion and discussed the influence of explosion pressure, number, and radius of released holes on the failure modes. Considering the influence of fluid-solid coupling and liquid jet, Wang et al. [33] investigated the fragmentation of ice subjected to the underwater explosion. Fan et al. [34,35] presented a coupling method between PD and SPH, and the soil fragmentation phenomenon caused by the shock wave of the buried explosive was numerically simulated.

In the present study, we focus on building a non-local model and approach to predict and investigate the failure characteristics of the concrete gravity dam subjected to underwater blast load. In particular, the meso-structural characteristics of concrete are taken into account through a modified IH-PD model [36–38], while the mechanical behavior of wet concrete is considered as well. After calibrated through two benchmark examples, the failure modes of the concrete gravity dam to underwater and air blast loads, and different explosion conditions, in terms of the TNT equivalent weight, standoff distance, and detonation depth, are conducted to investigate the effects have on the dynamic responses and failure modes of the concrete gravity dam.

The remains of this paper are organized as follows: In Section 2, the fundamentals of the peridynamic model and theory are briefly introduced. The peridynamic modeling for wet concrete is presented in Section 3. In Section 4, numerical verification of the peridynamic model is demonstrated, and the explosion failure of the concrete gravity dam is analyzed and discussed in Section 5. Conclusions are summarized in Section 6.

## 2. Methodology

### 2.1 Fundamentals of the ordinary state-based peridynamics

The motion equation in the ordinary state-based peridynamic theory [11] is given as follows:

$$\rho \ddot{\mathbf{u}}(\mathbf{x}, t) = \int_{H_{\mathbf{x}}} \{ \underline{\mathbf{T}}[\mathbf{x}, t] \langle \mathbf{x}' - \mathbf{x} \rangle - \underline{\mathbf{T}}[\mathbf{x}', t] \langle \mathbf{x} - \mathbf{x}' \rangle \} dV_{\mathbf{x}'} + \mathbf{b}(\mathbf{x}, t), \quad (1)$$

where  $\rho$  is the material density,  $\ddot{\mathbf{u}}$  is the acceleration of material point  $\mathbf{x}$ , and  $\mathbf{b}$  is the body force density of external load.  $\underline{\mathbf{T}}[\mathbf{x}, t]$  and  $\underline{\mathbf{T}}[\mathbf{x}', t]$  are force vector states of material points  $\mathbf{x}$  and  $\mathbf{x}'$ .  $dV_{\mathbf{x}'}$  denotes the volume for material point  $\mathbf{x}'$ . The integral domain  $H_{\mathbf{x}}$  is defined as  $H_{\mathbf{x}} = \{0 < |\mathbf{x} - \mathbf{x}'| < \delta\}$  (as shown in Fig. 1), where  $\delta$  is called horizon size.

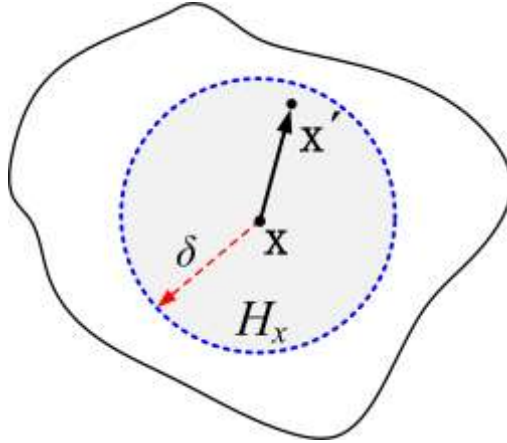


Fig. 1. The non-local interaction between material points.

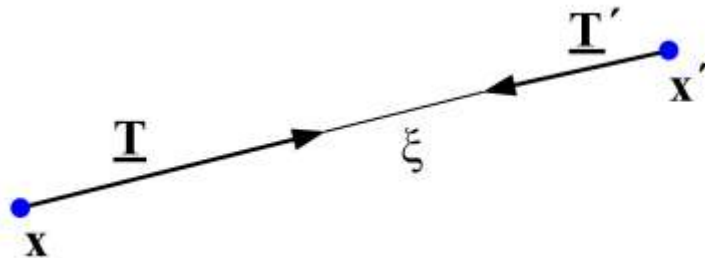


Fig. 2. Schematic of the ordinary state-based peridynamic model.

For ordinary state-based peridynamics, depicted in Fig.2, the force vector state  $\underline{\mathbf{T}}$

and the scalar state  $\underline{t}$  satisfies:

$$\underline{\mathbf{T}} = \underline{t} \underline{\mathbf{M}}, \quad (2)$$

where  $\underline{\mathbf{M}}$  is a unit vector for the deformed position of material points  $\mathbf{x}$  and  $\mathbf{x}'$ .

For the elastic material, the strain energy density  $W$  is given to be [11]:

$$W(\theta, \underline{e}^d) = \frac{k\theta^2}{2} + \frac{\alpha}{2} (\underline{\omega} \underline{e}^d) \cdot \underline{e}^d, \quad (3)$$

where  $k$  and  $\alpha$  are positive constants.  $\theta$  is a scalar valued function as the dilatation, and  $\underline{e}^d$  is the deviatoric part of the extension scalar state  $\underline{e}$ .

$$\begin{aligned} \underline{e} &= \underline{y} - \underline{x}, & \underline{y} &= |\underline{\mathbf{Y}}|, & \underline{x} &= |\underline{\mathbf{X}}| \\ \underline{e}^i &= \frac{\theta \underline{x}}{3}, & \underline{e}^d &= \underline{e} - \underline{e}^i \end{aligned} \quad (4)$$

$$\theta(\underline{e}) = \frac{3}{m} (\underline{\omega} \underline{x}) \cdot \underline{e}. \quad (5)$$

In Eq. (5),  $m$  denotes the weighted volume,

$$m = (\underline{\omega} \underline{x}) \cdot \underline{x}. \quad (6)$$

From Eq. (3), the scalar force state in Eq. (2) is denoted as:

$$\begin{aligned} \underline{t} &= \underline{t}^i + \underline{t}^d \\ &= \frac{\partial W}{\partial e^i} + \frac{\partial W}{\partial e^d} \\ &= \frac{3k\theta}{m} \underline{\omega} \underline{x} + \alpha \underline{\omega} \underline{e}^d \end{aligned} \quad (7)$$

## 2.2 Elastoplastic peridynamic model

An elastoplastic model in peridynamics was introduced in [39], where the strain energy density  $W$  is restated as:

$$W(\theta, \underline{e}^d, \underline{e}^{dp}) = \frac{k\theta^2}{2} + \frac{\alpha}{2} (\underline{e}^d - \underline{e}^{dp}) \cdot \omega (\underline{e}^d - \underline{e}^{dp}). \quad (8)$$

According to the above equation, the force state in Eq. (7) is rewritten as:

$$\begin{aligned}\underline{t} &= \underline{t}^i + \underline{t}^d \\ &= -\frac{3P}{m} \underline{\omega x} + \alpha \underline{\omega} (\underline{e}^d - \underline{e}^{dp}),\end{aligned}\quad (9)$$

where  $P = -k\theta$  denotes the peridynamic pressure.

The yield surface for the peridynamic elastoplastic model is defined here:

$$f = \frac{\|\underline{t}^d\|^2}{2} - \beta P - \varphi_0 \leq 0, \quad (10)$$

where  $\beta$  is the internal friction constant [40].

In this model, the plastic flow is assumed to be associated, which is defined as:

$$\underline{\dot{e}}^{dp} = \lambda \nabla^d f, \quad (11)$$

where  $\nabla^d f$  is the Frechet derivative, and  $\lambda$  denotes the consistency parameter. To satisfy the Kuhn-Tucker complementary conditions, the relation between the consistency parameter and the yield function is given as:

$$\lambda \geq 0, \quad f(t^d) \leq 0, \quad \lambda f(t^d) = 0. \quad (12)$$

### 2.3 The failure criterion in peridynamics

In peridynamics, one critical stretch criterion was proposed in [12], that once the bond stretch beyond a critical value, the bond is broken. When the bond breaks, there is no force sustainable, and cannot recover at all.

A history-dependent Boolean function is defined by:

$$\mu(t, \xi) = \begin{cases} 1 & s_0^{fc} < s(t', \xi) < s_0^{ft}, \quad 0 < t' < t \\ 0 & \text{else} \end{cases}, \quad (13)$$

where  $s$  is the bond stretch,  $s_0^{fc}$  and  $s_0^{ft}$  denote the critical stretches.

The local damage at any material point depends on the number of broken bonds (connected to that point), defined by:

$$D(\mathbf{x}, t) = 1 - \frac{\int_{H_{\mathbf{x}}} \mu(\xi, t) dV_{\mathbf{x}'}}{\int_{H_{\mathbf{x}}} dV_{\mathbf{x}'}}. \quad (14)$$

From Eq. (9), we note that  $0 \leq D \leq 1$ . If  $D$  is 0, means there is no damage, while 1 corresponds to the full damage at this point.

## 2.4 Numerical implementation

For numerical implementation, the motion equation in Eq. (1) is spatially discretized as:

$$\rho \ddot{\mathbf{u}}_i^n = \sum_p \mathbf{T}[\mathbf{x}_i^n, t^n] \langle \mathbf{x}_p^n - \mathbf{x}_i^n \rangle - \mathbf{T}[\mathbf{x}_p^n, t^n] \langle \mathbf{x}_i^n - \mathbf{x}_p^n \rangle V_p + \mathbf{b}(\mathbf{x}_i^n, t^n). \quad (15)$$

It is necessary to store the velocities and displacements for each material point at the current time-step and update them at the next time-step, and the explicit Verlet-Velocity algorithm is chosen in this study:

$$\begin{aligned} \dot{u}^{n+0.5} &= \frac{\Delta t}{2} \ddot{u}^n + \dot{u}^n \\ \dot{u}^{n+1} &= \frac{\Delta t}{2} \ddot{u}^{n+1} + \dot{u}^{n+0.5}, \\ u^{n+1} &= \Delta t \dot{u}^{n+0.5} + u^n \end{aligned} \quad (16)$$

where  $\Delta t$  is the time step size, and for stability, it should satisfy [10]:

$$\Delta t \propto \frac{\delta}{c'}, \quad (17)$$

where  $\delta$  denotes the size of horizon,  $c' = \sqrt{(\lambda' + 2\mu')/\rho}$  represents the dilatational wave speed,  $\lambda'$  and  $\mu'$  are the Lamé's elastic constants of the material.

## 3. The peridynamic modeling for wet concrete

Due to the water environment for concrete gravity dams, the water content in dams will be different after a long time. The mechanical properties of concrete will accordingly be influenced as well, in terms of the strength, strain rate effect, failure modes, etc. In this section, the peridynamic model for wet concrete is introduced in

detail.

### 3.1 Effective mechanical properties of wet concrete

In our previous study [38], the modified IH-PD model for concrete material was proposed (the implementation process is in Fig. 3). On the one hand, the heterogeneity characteristics of meso-structure are linked to the macroscopic model through the bond level, not considering the actual structure. On the other hand, the pore in concrete is represented in this model via the pre-broken bonds, where the effective bulk and shear modulus of concrete with a porosity  $\varphi$  are given by:

$$K^* = \frac{4K_m\mu_m(1-\varphi)}{(4\mu_m + 3K_m\varphi)}, \quad (18)$$

$$\mu^* = \mu_m(1-\varphi^2)$$

where  $K_m, K^*$  is the original and effective bulk modulus,  $\mu_m$  and  $\mu^*$  is the original and effective shear modulus.

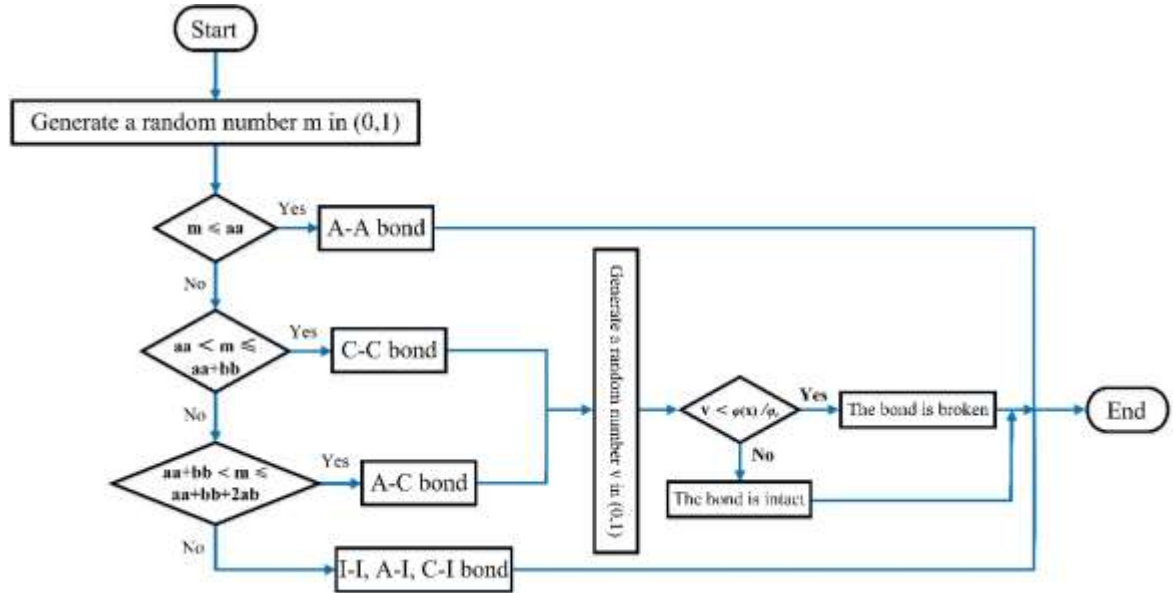


Fig. 3. The flowchart of a pre-processing algorithm for the IH-PD model considering concrete pores.

To depict the effect pore water has on the mechanical property of wet concrete, an equivalent relationship is established between the pore water and porosity. The bulk modulus of pore water is assumed to be  $K_w$  ( $K_w < K_m$ ). As shown in Fig. 4, an

equivalent two-phase model is constructed [41], indicating that  $K_w$  is identical to the effective bulk modulus of concrete with porosity  $\varphi_1$  :

$$K_w = \frac{4K_m\mu_m(1-\varphi_1)}{4\mu_m + 3K_m\varphi_1}. \quad (19)$$

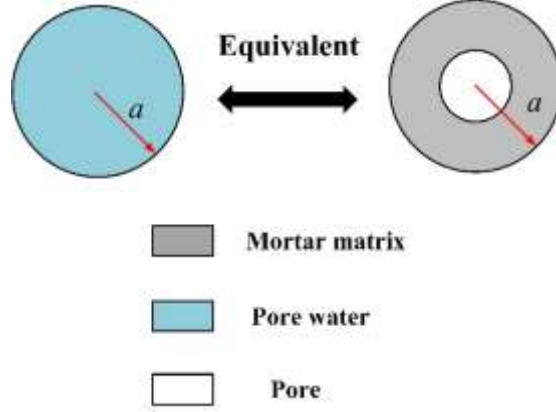


Fig. 4. The equivalent model of pore water and mortar matrix with a pore.

According to the foregoing equivalent principle, the effective bulk modulus in saturated concrete and unsaturated concrete is given in the following equations, respectively. More details are specifically introduced in [42]. Besides, the shear resistance of common water could be negligible. Nevertheless, except for the inertia effect on the shear resistance of wet concrete, the effect viscosity of pore water has on it cannot be neglected as well.

$$K_1^* = \frac{4K_m\mu_m \left( 1 - \left( \frac{1-\varphi}{1-\varphi \cdot w} \right) \right)}{4\mu_m + 3K_m \cdot \left( \frac{\varphi - \varphi \cdot w}{1-\varphi \cdot w} \right)}, \quad \mu_1^* = \mu_m \left( 1 - \left( \frac{\varphi - \varphi \cdot w}{1-\varphi \cdot w} \right)^2 \right), \quad (20)$$

$$K_{sat}^* = \frac{4K_m\mu_m(1-\varphi_2)}{4\mu_m + 3K_m\varphi_2} = \frac{4K_m\mu_m(1-\varphi\varphi_1)}{4\mu_m + 3K_m\varphi\varphi_1}, \quad (21)$$

$$\mu_{sat}^* = (1 + f_1\varphi^2 + f_2\varphi)(1-\varphi^2)\mu_m$$

$$K_{unsat}^* = \frac{4K_1^* \mu_1^* (1 - \varphi_2)}{4\mu_1^* + 3K_1^* \varphi_2} = \frac{4K_1^* \mu_1^* \left(1 - \left(\varphi_{sat} + \frac{1}{2}\varphi_{unsat}\right)\varphi_1\right)}{4\mu_1^* + 3K_1^* \left(\varphi_{sat} + \frac{1}{2}\varphi_{unsat}\right)\varphi_1} = \frac{4K_1^* \mu_1^* (1 - \varphi \cdot w \cdot \varphi_1)}{4\mu_1^* + 3K_1^* \varphi \cdot w \cdot \varphi_1}, \quad (22)$$

$$\mu_{unsat}^* = \mu_1^* \left(1 - \left(\varphi_{sat} + \frac{1}{2}\varphi_{unsat}\right)^2\right) = \mu_1^* (1 - (\varphi \cdot w)^2)$$

where  $w$  is the saturation of wet concrete.

### 3.2 Dynamic model for wet concrete

Due to the existence of pore water inside wet concrete, the unconfined strength of wet concrete is found to be slightly lower than that of dry concrete from the experimental observations. According to this phenomenon, one empirical equation for the wet concrete strength is presented by Zhao [43] as follows:

$$\begin{aligned} \frac{f_c^w}{f_c} &= -0.2w + 1.0 \\ \frac{f_t^w}{f_t} &= -0.2w + 1.0 \end{aligned}, \quad (23)$$

where  $f_c$ ,  $f_t$  denotes the compressive and tensile strength of dry concrete, and  $f_c^w$ ,  $f_t^w$  is the compressive and tensile strength of wet concrete.

The critical tensile and compressive stretch in Eq. (13) for wet concrete is presented as:

$$\begin{aligned} s_0^{ft} &= f_t^w / E_w, & s \geq 0 \\ s_0^{fc} &= f_c^w / E_w, & s < 0 \end{aligned}, \quad (24)$$

From the experimental observations [44,45], it is found that wet concrete is much more sensitive to the strain rate than dry concrete, especially when subjected to blast load. To represent the dynamic mechanical response of wet concrete, an empirical formula is presented as:

$$g_t(\dot{s}_t, w) = \frac{DIF_t^w}{DIF_t^{dry}} = \begin{cases} 1, & \dot{s}_t \leq 10^{-5} \\ -A^{-\lg \dot{s}_t} + 2, & \dot{s}_t > 10^{-5} \end{cases}, \quad (25)$$

$$g_c(\dot{s}_c, w) = \frac{DIF_c^w}{DIF_c^{dry}} = \begin{cases} 1, & \dot{s}_c \leq 10^{-5} \\ \frac{DIF_t^w \cdot f_t^{dry} / f_c^{dry} + 1}{DIF_t^{dry} \cdot f_t^{dry} / f_c^{dry} + 1}, & \dot{s}_c > 10^{-5} \end{cases}, \quad (26)$$

where  $A$  is a material parameter, and it satisfies:

$$A = 1 + HW, \quad (27)$$

where the value  $H$  is 0.15.

According to Eq. (25) and Eq. (26), the dynamic increase factor of wet concrete can be denoted as:

$$DIF_c^w = [1 + C \ln(\dot{s}_c)] \cdot g_c(\dot{s}, w)$$

$$DIF_t^w = \begin{cases} \left( \frac{\dot{s}_t}{\dot{\epsilon}_t} \right)^\zeta, & \dot{s} \leq 10^{-5} \\ \left( \frac{\dot{s}_t}{\dot{\epsilon}_t} \right)^\zeta \cdot g_t(\dot{s}, w), & 10^{-5} < \dot{s}_t \leq 30s^{-1} \\ \beta \left( \frac{\dot{s}_t}{\dot{\epsilon}_t} \right)^{\frac{1}{3}} \cdot g_t(\dot{s}, w), & \dot{s}_t > 30s^{-1} \end{cases}, \quad (28)$$

where  $C$ ,  $\zeta$ ,  $\beta$  are positive constants.

The pore water can stay in pores and bear partial hydrostatic pressure, thus the hydrostatic pressure in wet concrete  $P'$  is given by:

$$P' = P_{dry} + bP_w, \quad (29)$$

$$P_{dry} = k_1 \bar{\mu} + k_2 \bar{\mu}^2 + k_3 \bar{\mu}^3, \quad (30)$$

$$P_w = \frac{\rho_0 L^2 \mu' \left( 1 + \left( 1 - \frac{\gamma_0}{2} \right) \mu' - \frac{\alpha}{2} \mu'^2 \right)}{1 - (S_1 - 1) \mu' - S_2 \frac{\mu'^2}{\mu' + 1} - S_3 \frac{\mu'^3}{(\mu' + 1)^2}} + (\gamma_0 + \alpha \mu') E, \quad (31)$$

where  $P_{dry}$  and  $P_w$  denotes the solid and free water part of the hydrostatic pressure [46].

Other details could be found in [42].

## 4. Numerical verification

In this section, results from experimental observations and numerical simulations are presented in terms of the failure modes of concrete targets subjected to air and underwater blast load, respectively. The subsequent verification of peridynamic model for such explosion damage and failure is established.

### 4.1 A reinforced concrete slab subjected to air blast load

In this section, the explosion failure of a reinforced concrete slab subjected to air blast load is numerically studied. The corresponding geometry and loading condition are selected to be identical to experimental tests in [47]. Fig. 5 illustrates the schematic diagram of peridynamic model. The reinforced concrete slab has a span of 1000 mm with a thickness of 100 mm. The slab is reinforced with 10 mm diameter steel bars, which are arranged uniformly with a constant spacing of 100mm. The weight of explosive is 1.62kg, which is equivalent to 1.0kg TNT. The standoff distance between explosive charge and reinforced concrete slab is 100mm.

From the experimental setup, the compressive strength of concrete and cement mortar is assigned to be 47MPa and 42.5MPa, and the strength of aggregate and ITZ is assumed to be 125MPa and 38MPa, respectively. Other material properties of each phase in concrete are given in Table 1 [48]. The density of steel bars is 7860kg/m<sup>3</sup>. Since the blast load from 1.0kg TNT is far less than the yield strength of steel bars, the explosion failure mainly occurs on concrete other than steel bars. The yield strength of steel bars is 350GPa. For peridynamic modeling, the horizon size  $\delta$  is 8mm, and uniform discretization is used here  $\delta=3\Delta x$ . The total number of nodes is 264,850.

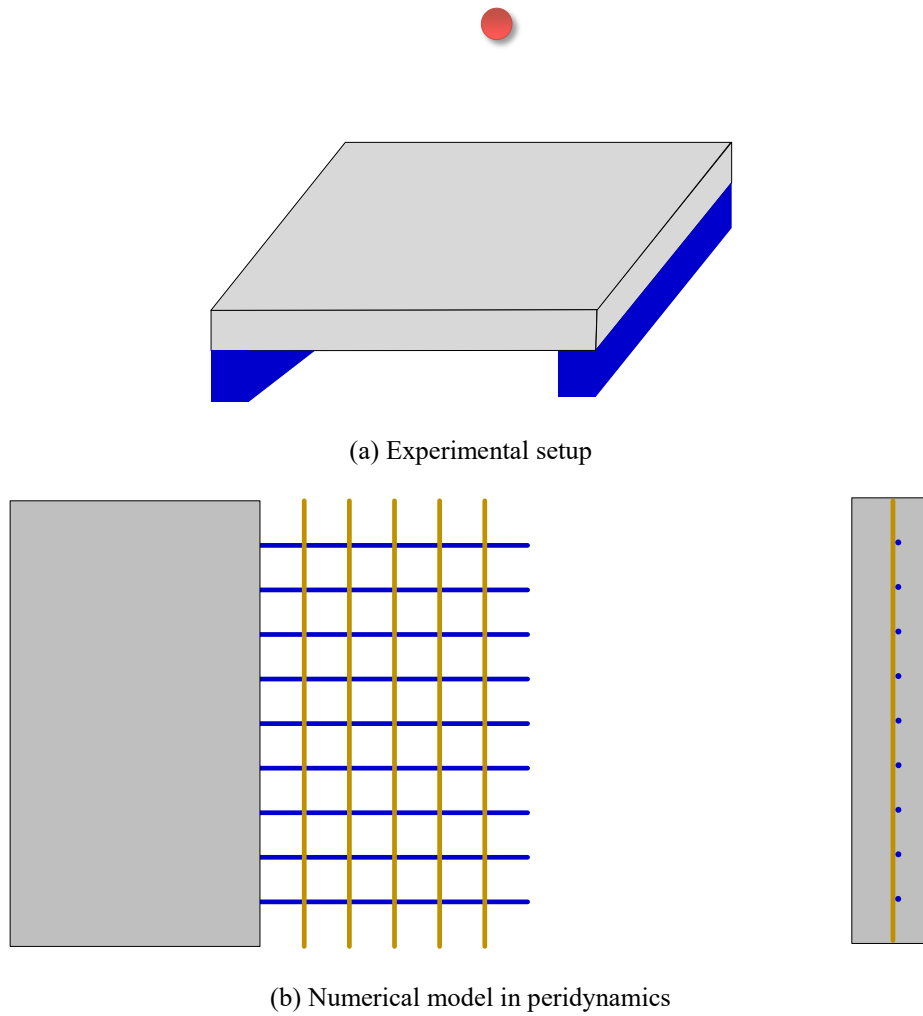


Fig. 5. The geometric model for explosion failure of the reinforced concrete slab.

Table. 1 The material property of each phase in concrete.

Concrete phase	Young's modulus (GPa)	Fracture energy (N/m)
concrete	35.7	107.0
aggregate	63.0	365.0
cement mortar	29.3	110.0
ITZ	22.5	60.0

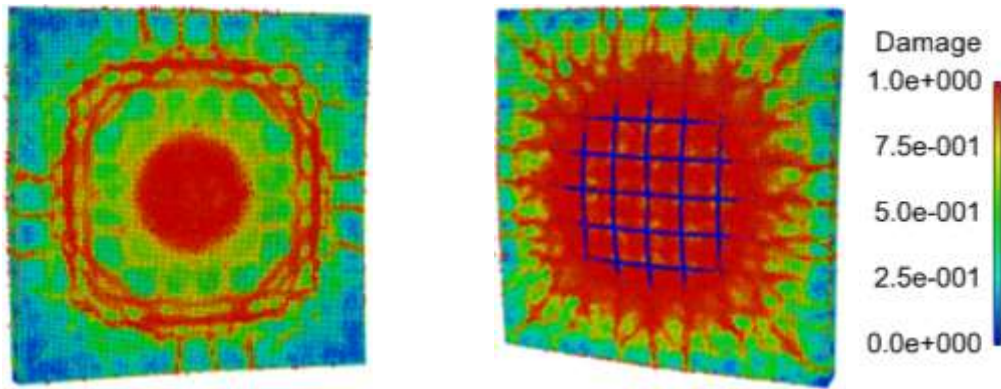
The explosion failure modes for the reinforced concrete slab from experimental observations and numerical simulations are presented in Fig. 6. There is a satisfactory agreement on the actual and predicted results. According to Fig. 6, typical cratering and scabbing failures are found on the outer and back surfaces of the slab. Several visible and disordered cracks are observed at the outer surface, while much more radial cracks

propagate from the center region. Due to the severe scabbing failure, uncovering steel bars could be observed from the view of the back surface. Besides, the average size of the failure region at outer and back surfaces, measured in experimental test, was 381mm (15 inches) and 736.6mm (29 inches) [47], and predicted ones obtained by peridynamic simulation are 340.55mm and 707.64mm.

Nevertheless, it should be noted that there are still some slight discrepancies between numerical results and experimental data. On the one hand, predicted results for the failure region are a bit smaller than that measured from experimental tests. One corner of the slab is totally damaged and disappeared during the explosion process, but this phenomenon is not numerically depicted here. On the other hand, several evident circular cracks propagate at the outer surface, which is not observed in experimental measurements. The perhaps reason for these discrepancies is the treatment method for the boundary condition. In the experimental setup, the slab is fixed by four curved steel bars at the back surface (shown in Fig. 6(a)), and yet we just fixed the displacement for the slab along the direction of blast load in numerical simulations.



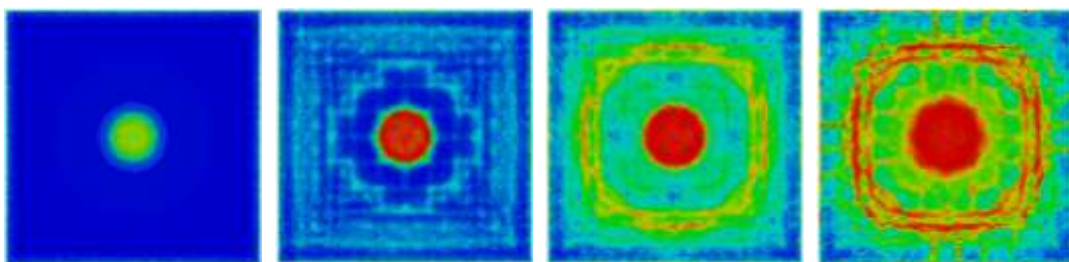
(a) Experimental observations



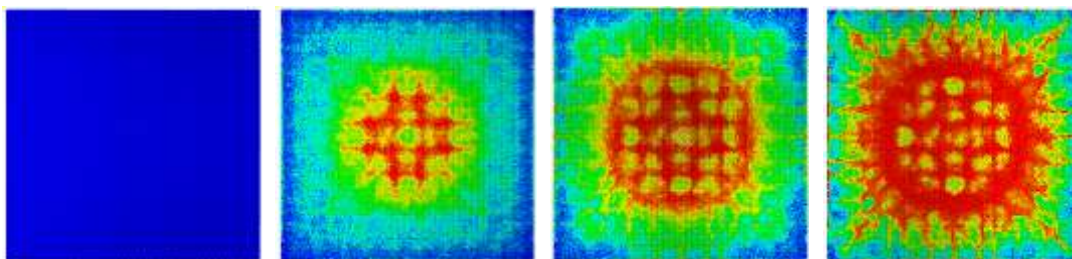
(b) Peridynamic predictions

Fig. 6. Damage maps of reinforced concrete slab subjected to blast load, left: outer surface and right: back surface.

The damage evolution in time sequence for outer and back surfaces to blast load is illustrated in Fig. 7. Once the blast shock wave arrives at the slab, explosion damage immediately occurs at the outer surface, meaning the explosion pressure is much greater than the compressive strength of the concrete. On account of the tensile stress at the back surface, reflected from the compressive stress when it propagates to the back surface, the tensile damage is soon developed. Meanwhile, the compressive stress propagates and reflects horizontally at the outer surface, and the typical circular cracks occur and propagate gradually as well.



(a) Outer surface



(b) Back surface

Fig. 7. Damage evolution in time sequence of the reinforced concrete slab.

#### 4.2 A scaled concrete dam subjected to underwater blast load

In this section, a scaled concrete gravity dam under an underwater explosion was modeled and numerically analyzed. The numerical model is identical to the Vanadit-Ellis and Davis experimental tests [49] (presented in Fig. 8), where the dam target was placed in a steel container, and whole tests were conducted in a large centrifuge. As shown in Fig. 9, we only consider the gravity dam part in the numerical study, with certain boundary conditions enforced on the bottom steel plate. For the numerical simulation in [1], the equivalent TNT weight is 8g and the explosion charge is under the water surface of 0.025m. The same blast condition is employed in this study.

The compressive strength of concrete is assigned to be 34.5MPa according to test data, and the strength of aggregate, cement mortar, and ITZ is assumed to be 92MPa, 30MPa, and 28MPa, respectively. Other material properties of each phase in concrete are given in Table 2. The density of steel plate is  $7800\text{kg/m}^3$ , and the yield strength is 210GPa. For peridynamic modeling, the horizon size  $\delta$  is 8mm, and uniform discretization is used here  $\delta=3\Delta x$ . The total number of nodes is 287,073.

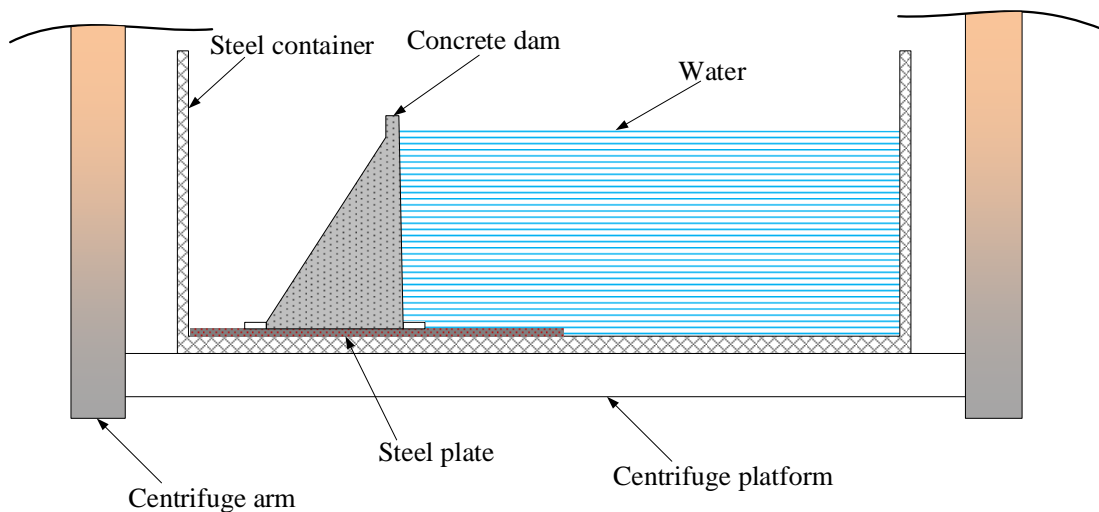


Fig. 8. Schematic diagram for the experimental tests.



Fig. 9. Numerical model of the gravity dam in peridynamics.

Table. 2 The material property of each phase in concrete.

Concrete phase	Young's modulus (GPa)	Fracture energy (N/m)
concrete	49.19	105.0
aggregate	86.33	360.0
cement mortar	40.0	108.0
ITZ	36.7	59.0

The final failure patterns of the gravity dam obtained with the experimental tests and peridynamic simulations are depicted in Fig. 10. The difference between two cases is the standoff distance, which is shorter in the first case than the second one. The results shown in Fig. 10 demonstrate a reasonable agreement for numerically predicted ones and experimental measurements.

When the blast charge is very close to the upstream slope, the underwater explosion pressure is greater than the concrete strength. Once the blast shock wave arrives at the concrete dam, the concrete fails from crushing and spalling. There is a clear blast gap in Fig. 10(a). This failure pattern is referred to as the dam material failure. For the greater standoff distance, the explosion pressure applied to the dam is too low to cause the immediate failure of concrete. Under the sustained blast load, the dam gradually fails from the concrete tensile and shearing failure. This “punching shear” mode is

referred to as the dam localized failure, shown in Fig. 10(b).

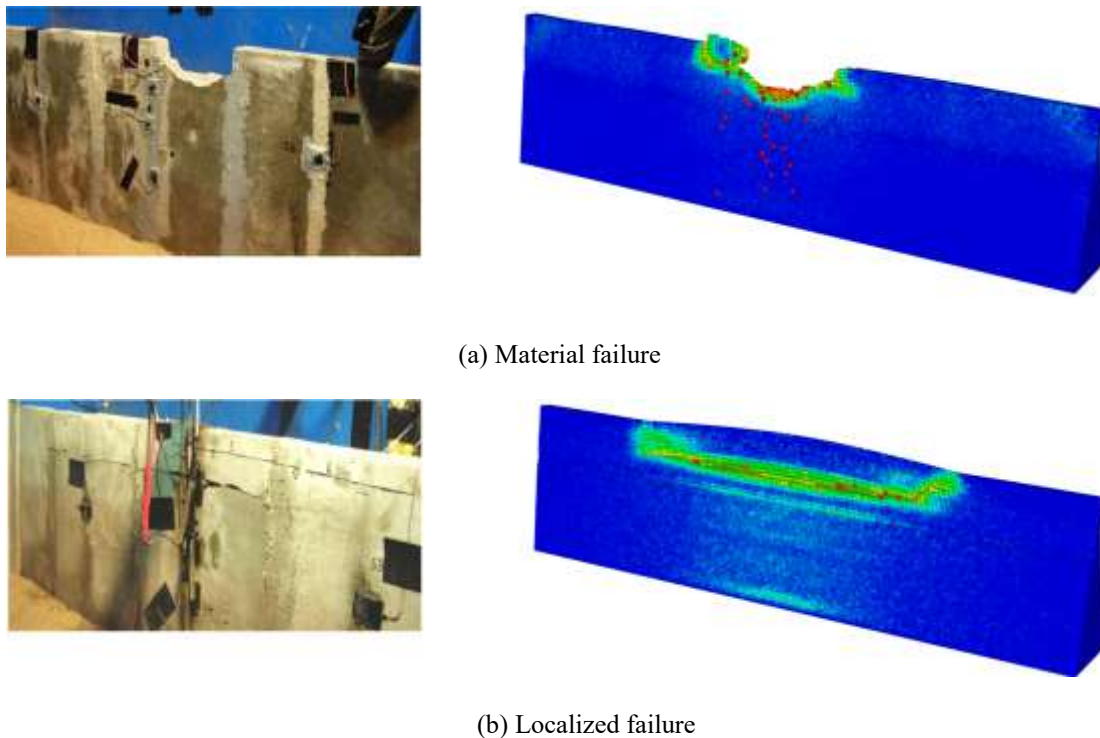


Fig. 10. Failure patterns of the gravity dam to underwater blast load, left: experimental observations, right: peridynamic numerical prediction.

## 5. Results and discussion

One typical gravity dam is numerically analyzed in this section, as presented in Fig. 12. The width of dam crest and bottom are 16m and 122m. The total height of the dam is 159m, where the elevation of upstream water surface is 149m, and the value of downstream is 40m. To reduce the calculation cost, the longitudinal depth of dam ( $z$ -direction) is only chosen to be 1.5m. The boundary condition set here is that the upstream and downstream faces of dam are fixed in the horizontal ( $x$ ) direction, and the bottom of dam is fixed both in the horizontal ( $x$ ) and vertical ( $y$ ) direction. For a better understanding of the explosion response of the gravity dam, four monitoring points are arranged on the upstream face, as shown in Fig. 13. Point A is at the center of the dam crest, point B at the upstream water surface, and points C and D are at underwater 70m and 110m, respectively.

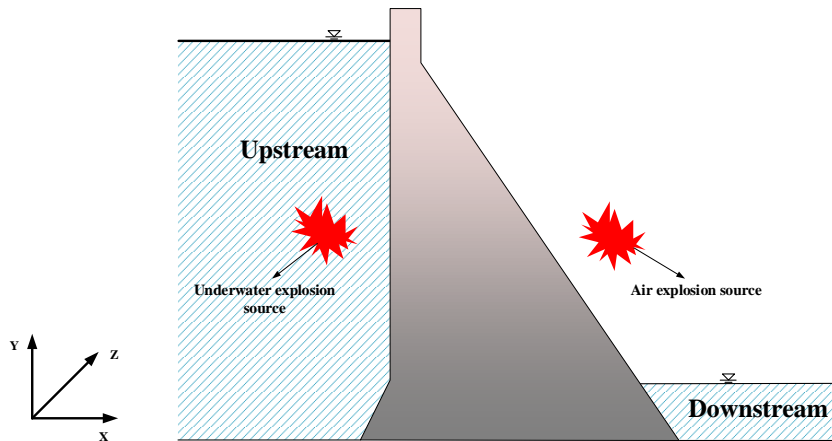


Fig. 12. Schematic diagram of the gravity dam model

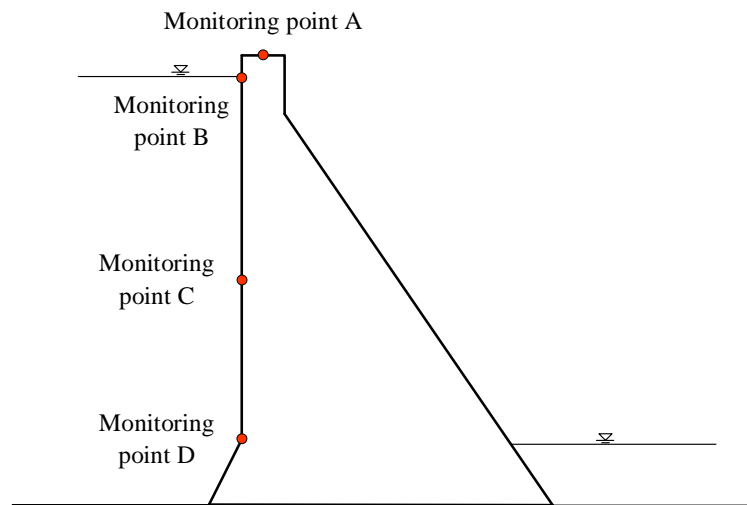


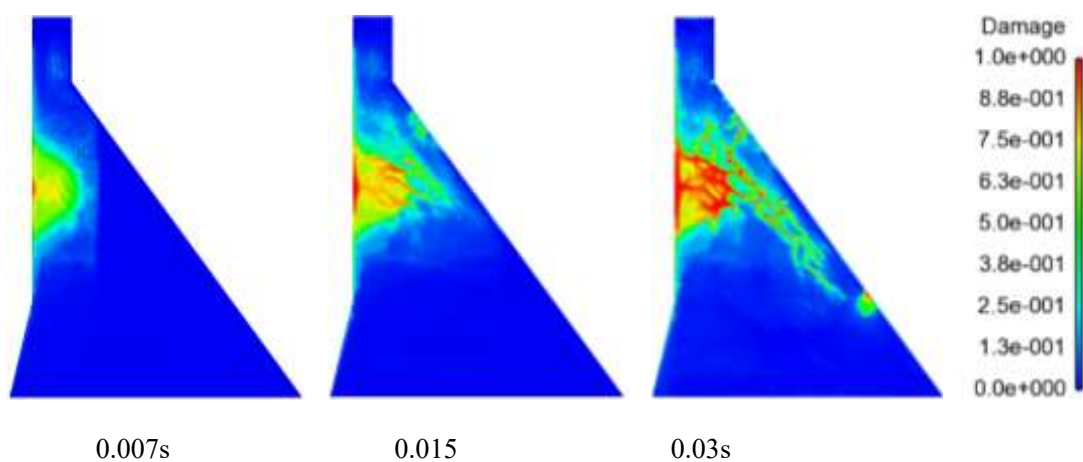
Fig. 13. Distribution of monitoring points in the gravity dam

### 5.1 Explosion response of dam to underwater and air blast load

In this section, we mainly study the explosion failure of the gravity dam subjected to underwater and air blast loads, respectively. The detonation depth is 47m below the upstream water surface, and the standoff distance is 10m. The weight of explosive is equivalent to 1000kg TNT. The internal porosity of concrete is 6%, the saturation is 80%, and the compressive strength of concrete is 39.5 MPa. The material properties of concrete are identical to the values employed in the previous case. In the peridynamic simulation, the horizon size is 0.9m, and 3 times the grid spacing  $\delta = 3\Delta x$ . There is a total of 595,383 material points.

Fig. 14 and Fig. 15 show the explosion failure modes of the dam when subjected

to underwater and air blast load, respectively. It can be seen from Fig. 14 that when the detonation shock wave meets the upstream face, explosion failure immediately occurs and a severe blasting pit is developed. As the shock wave propagates to the downstream face, the tensile stress is reflected from the compressive stress. The tensile damage is soon developed on the downstream face and then evolves into several macroscopic cracks. Besides, several oblique cracks can be found between the blasting pit and downstream face as well, and their directions are parallel to the downstream face. It is worth noting that the cracks initiated at the end of the blasting pit intersect with oblique cracks and no longer propagate towards the downstream face. Moreover, one crack appears at the upstream heel of the dam and gradually propagates along the foundation surface, which may have a great effect on the safety performance of the gravity dam. For the explosion response of the dam to the air blast load, only a few damaged areas are observed on the downstream face, which is quite different from the results of the underwater blast load. We can conclude that for the same explosion conditions, the shock wave intensity generated by the underwater explosion is significantly greater than that generated by the air explosion.



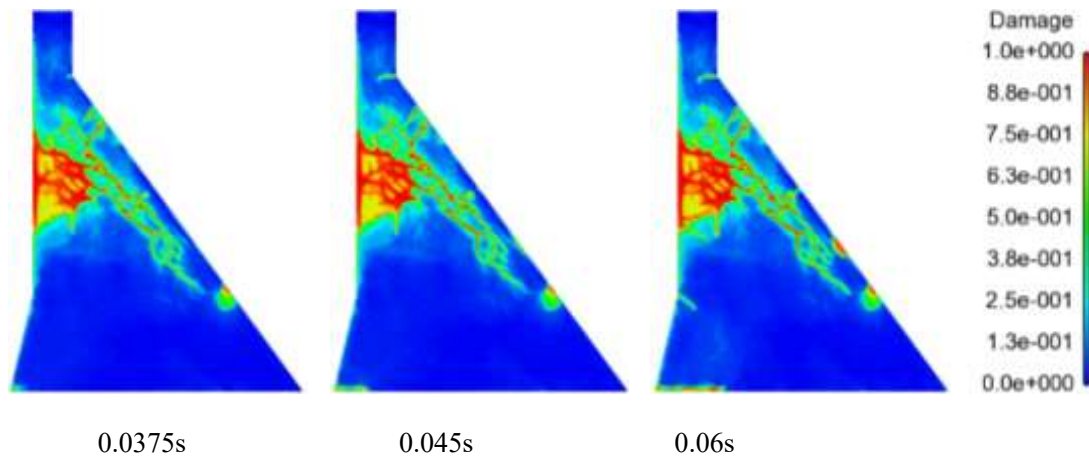


Fig. 14. Failure patterns of gravity dam subjected to underwater blast load.

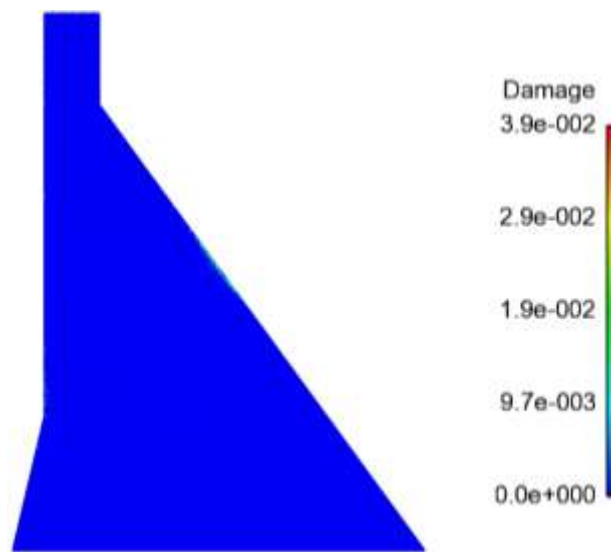


Fig. 15. Damage pattern of gravity dam subjected to air blast load.

The displacements of the gravity dam in the x and y directions are shown in Fig. 16. From Fig. 16, we can see that the shock wave, generated by the underwater explosion, acts on the upstream face and spreads rapidly to the downstream face. When the shock wave reaches the downstream face, the compressive stress wave is reflected to be the tensile stress wave, and the cracks occur gradually in the downstream face. Then, the tensile stress wave continues to propagate towards the upstream face and overlaps with the compressive stress wave, as shown in Fig. 16 at 0.01s. With the interaction of compressive and tensile stress waves, the oblique cracks initiate and propagate in the intersection area, as depicted in Fig. 16 at 0.015s and 0.02s.

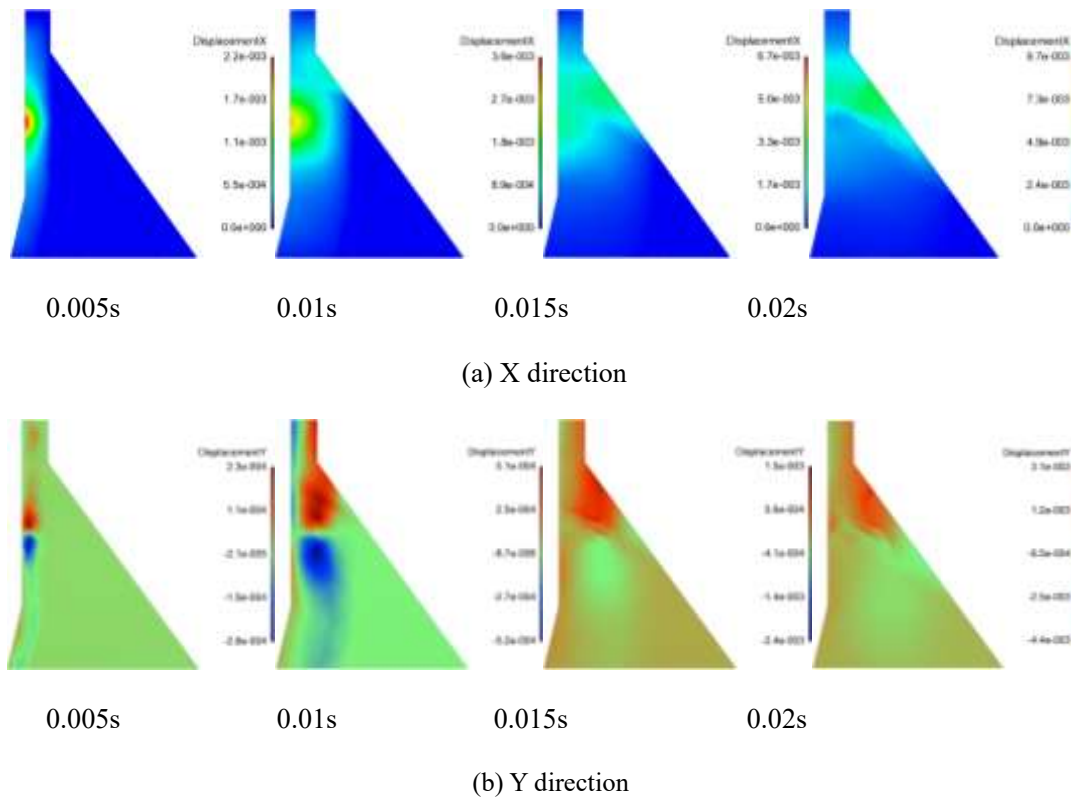
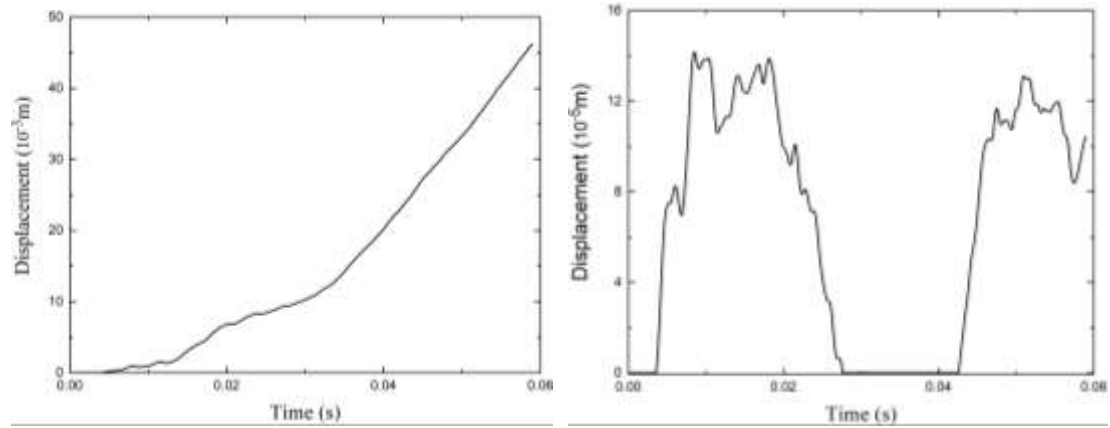


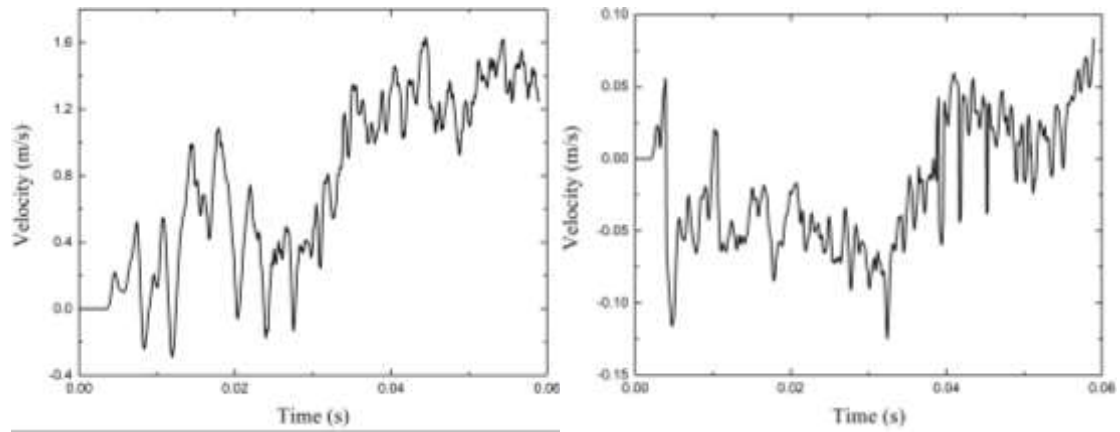
Fig. 16. Displacement variation of gravity dam under underwater blast load.

To have a better study on the dynamic response of the gravity dam to underwater and air explosions, the displacement, velocity, and acceleration of monitoring point A (at the top of the dam) are analyzed and discussed. The predicted results are shown in Fig. 17, 18, and 19. The maximum displacement of the dam crest is 46.1mm and 0.14mm under underwater and air explosion. Besides, the maximum velocity and acceleration of dam crest are 1.63m/s and 1813.57m/s<sup>2</sup> in underwater explosion, while the value of air explosion is 0.126 m/s and 203.95 m/s<sup>2</sup>. From these results, it is obvious that the explosion failure of the gravity dam subjected to underwater blast load is more serious than that of air blast load, and the dynamic response of the gravity dam is more intense as well.



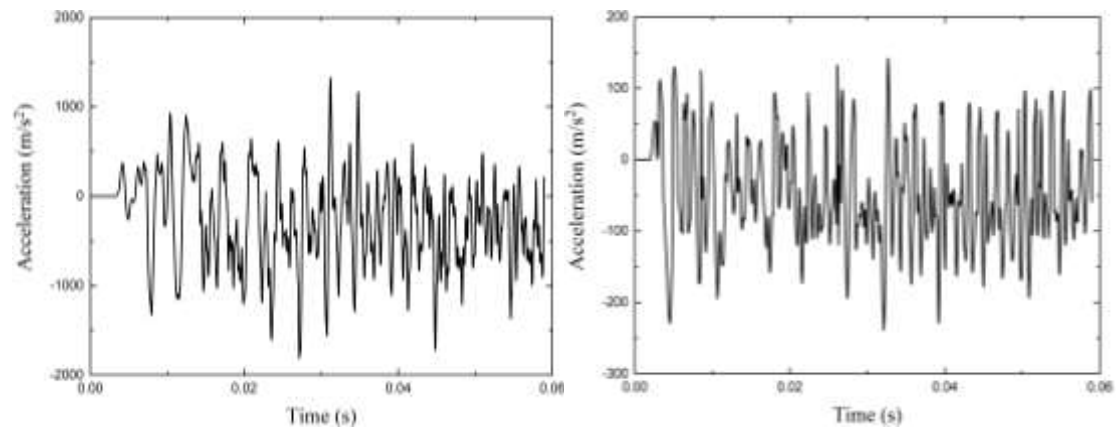
(a) Underwater explosion (b) Air explosion

Fig. 17 Displacement time histories for dam crest point.



(a) Underwater explosion (b) Air explosion

Fig. 18 Velocity time histories for dam crest point.



(a) Underwater explosion (b) Air explosion

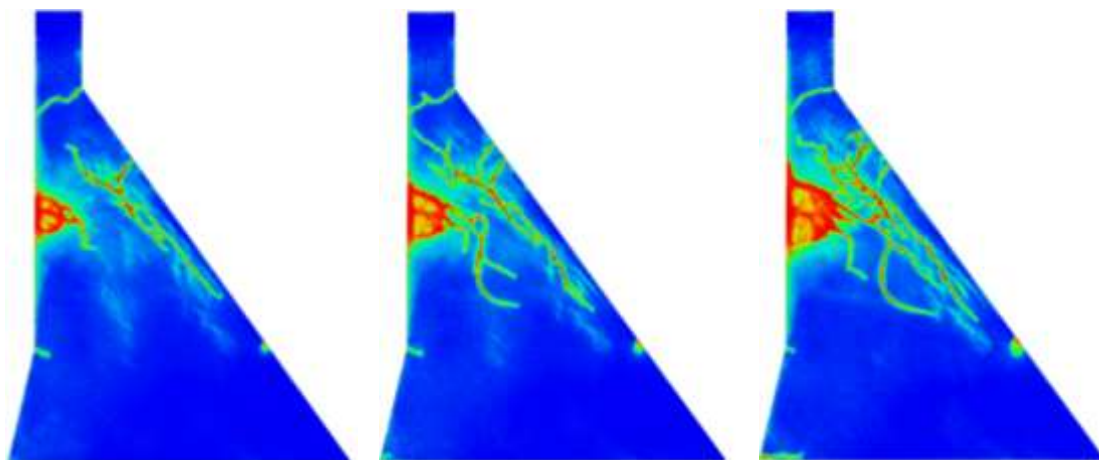
Fig. 19 Acceleration time histories for dam crest point.

## 5.2 Failure analysis of gravity dam with different underwater explosion conditions

According to the aforementioned section, it is found that the explosion response of

gravity dams is particularly more intense during the underwater explosion. To further study the influence of different conditions on the failure mode of gravity dam to underwater blast load, the explosion equivalent, standoff distance, and detonation depth are chosen to be variables in this section.

Firstly, five different cases are conducted with various explosion equivalent, 350kg, 500kg, 750kg, 1000kg, and 2000kg. The standoff distance is 10m, and the detonation depth is 47m below the upstream water surface. The explosion failure modes of the dam with different explosion equivalents are shown in Fig. 20. Although the explosion equivalent is different, the failure modes of the dam are nearly similar to each other, which mainly include the blasting pit on the upstream face, the macroscopic cracks on the downstream face, and the oblique cracks in the intersection area. Nevertheless, with the increase of explosion equivalent, the size of the blasting pit enlarges significantly, and the number of macroscopic and oblique cracks increases as well. The sizes of blasting pits with different explosion equivalents are depicted in Fig. 21. Besides, when the explosion equivalent is 500kg, the crack near the upstream heel begins to initiate but does not propagate continuously. Once the explosion equivalent is more than 500kg, the crack propagates to the downstream face along the foundation surface.



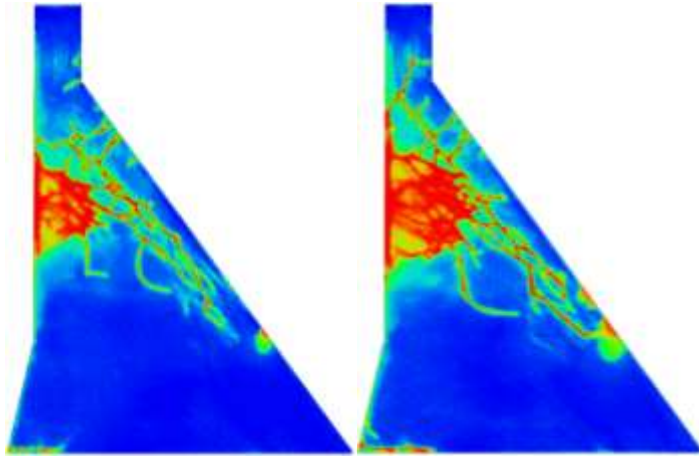


Fig. 20. Failure pattern of gravity dam with different explosive weights.

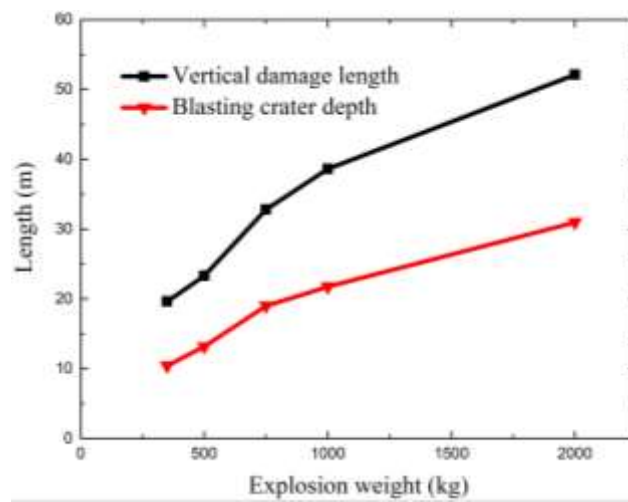


Fig. 21. Blasting crater depth and vertical damage length of gravity dam with different explosive weights.

The peak accelerations of the gravity dam with different explosion equivalents are presented in Fig. 22. We can see that if the explosion equivalent is larger, the blast load pressure to the dam is higher, and the peak acceleration of the dam is much greater. When the explosion equivalent is less than 1000kg, the peak acceleration curve has almost linear growth. While the explosion equivalent is greater than 1000kg, the growth rate of the peak acceleration curve decreases significantly.

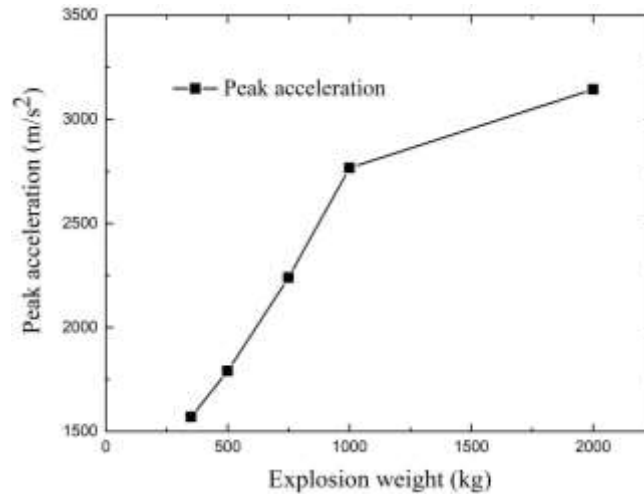


Fig. 22. Peak acceleration of dam under different explosive quantities.

To study the influence of standoff distance on the explosion failure mode of the gravity dam, four different standoff distances of 5m, 10m, 20m, and 40m are simulated. The explosion equivalent is 1000kg, and the denotation depth is 47m below the upstream water surface.

Fig. 23 shows the failure modes of the dam with different standoff distances predicted in this study. It is clear that the standoff distance has a great influence on the failure mode of the gravity dam. When the standoff distance is 5m, the top and middle regions of the dam fail seriously, and the blasting pit intersects with the oblique cracks. With the standoff distance of 10m, it can be observed that the failure region becomes much smaller, and the oblique cracks initiate and propagate between the blasting pit and the downstream slope. When the standoff distance is 20m, only a small blasting pit is developed near the explosion source. Moreover, there is only one oblique crack could be observed. No cracks occur near the upstream heel except the damaged area. For the standoff distance of 40m, there are only a few damaged areas, and no blasting pit and cracks are observed, meaning the dam integrity is not affected.

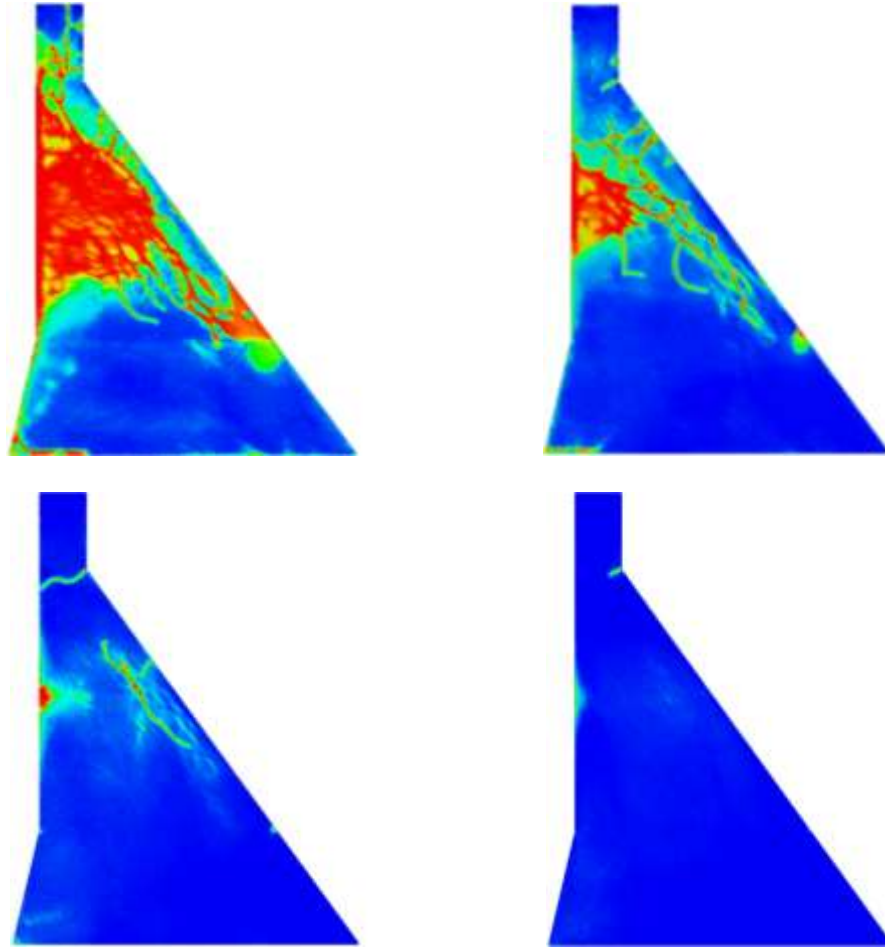


Fig. 23. Failure pattern of gravity dam under different standoff distances.

The sizes of blasting pits with different standoff distances are shown in Fig. 24. The pit depth and vertical height decrease prominently with the increase of standoff distance, and their variation rate also decreases gradually. When the standoff distance exceeds 20m, the curve tends to be steady, indicating that the detonation pressure load is slight, and the dam can maintain great integrity. Fig. 25 illustrates the peak acceleration curve of the dam, which decreases exponentially with the increase of standoff distance.

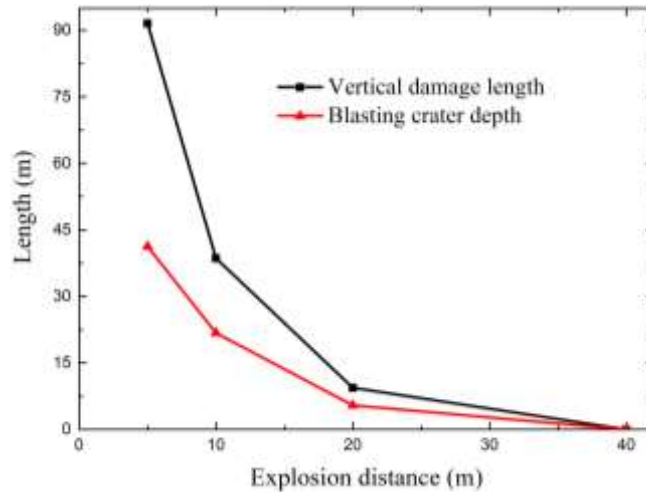


Fig. 24. Blasting crater depth and vertical damage length of gravity dam with different standoff distances.

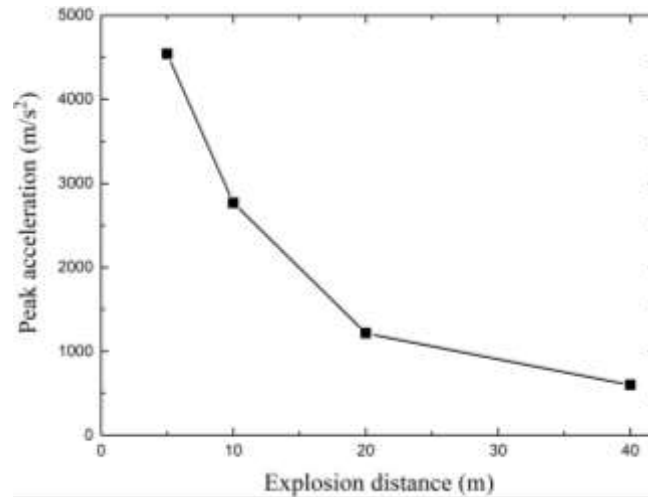


Fig. 25. Peak acceleration of dam with different standoff distances.

Finally, the failure modes of the dam with three different denotation depths are simulated and analyzed, which are 10m, 47m, and 82m below the upstream water surface. The explosion equivalent and standoff distance are 1000kg and 10m. Fig. 26 shows the numerical results with different denotation depths. When the denotation depth is 10m, the crest area is seriously failed. However, other areas are safe, with only several oblique cracks near the downstream and a horizontal crack at the corner of the upstream face. When the initiation depth is 47m and 92m, the failure modes are similar, including the blasting pit and oblique cracks. And several cracks around the blasting pit

would interest the oblique cracks. Moreover, it is worth noting that there is one crack near the upstream heel only when the denotation depth is 47 m among these conditions. Although the explosion source is close to the upstream heel when the initiation depth is 92m, there is still only a damaged area and no crack occurs.

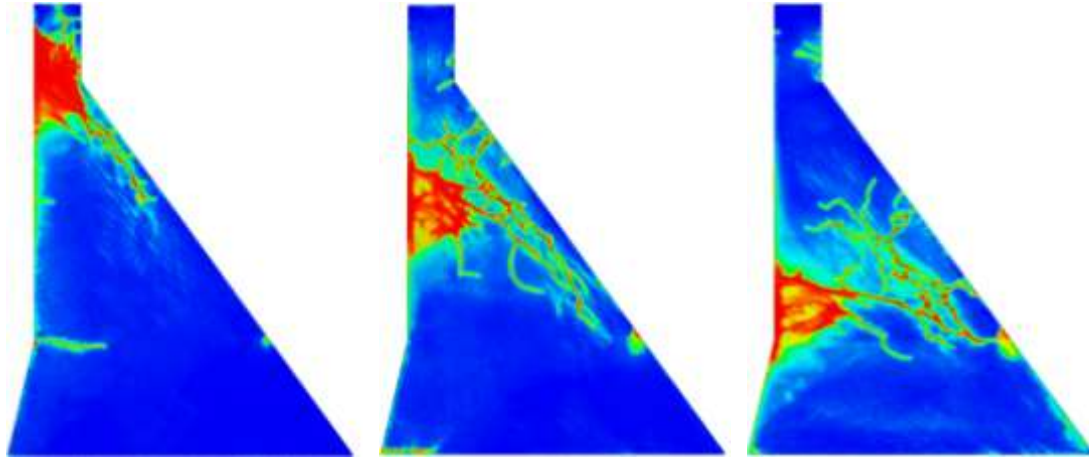


Fig. 26. Failure patterns of gravity dam with different denotation depths.

The peak accelerations of the dam with different denotation depths are listed in Table 3. It can be seen that the peak accelerations at three denotation depths do not change dramatically, demonstrating that the failure modes of the dam are different with different denotation depths, but the dynamic responses are not greatly influenced.

**Table 3 Peak acceleration of dam under different denotation depths.**

Denotation depth	Peak acceleration
10m	2787.50m/s <sup>2</sup>
47m	2767.12m/s <sup>2</sup>
92m	2600.22m/s <sup>2</sup>

## 6. Conclusion

The explosion failure of concrete gravity dam to underwater blast load is analyzed by peridynamics in this study. The meso-structural characteristics of concrete are taken into account through a modified IH-PD model, and the mechanical behavior of wet concrete is considered as well. The intact failure process of the dam, when subjected to

the underwater explosion, is numerically simulated, and the effects of explosion equivalent, standoff distance, and detonation depth on failure modes of the dam are discussed respectively. The main conclusions are as follows:

(1) Two benchmark examples for the blast-induced failure of concrete are investigated, numerical results illustrate that the peridynamics model and method are capable of characterizing the dynamic behavior and explosion failure of concrete.

(2) With the same explosion conditions, in terms of the explosion equivalent, standoff distance, and denotation depth, the explosion failure of the gravity dam to underwater blast load is particularly more severe than that to air blast load, and the dynamic response is much more intense as well.

(3) The specific effects of the explosion equivalent, standoff distance, and denotation depth have on the failure modes of the gravity dam are discussed, and the numerical results are valuable for the safe operation and protection design of the concrete gravity dam.

## **References**

- [1] Wang X, Zhang S, Wang C, Cui W, Cao K, Fang X. Blast-induced damage and evaluation method of concrete gravity dam subjected to near-field underwater explosion. *Eng Struct* 2020;209:109996.
- [2] Shu Y, Wang G, Lu W, Chen M, Lv L, Chen Y. Damage characteristics and failure modes of concrete gravity dams subjected to penetration and explosion. *Eng Fail Anal* 2022;134:106030.
- [3] Zhu J, Chen Y, Lyu L. Failure analysis for concrete gravity dam subjected to underwater explosion: A comparative study. *Eng Fail Anal* 2022;134:106052.
- [4] Hughes TJR. *The finite element method: linear static and dynamic finite element analysis*. Courier Corporation; 2012;

- [5] Masi F, Stefanou I, Maffi-Berthier V, Vannucci P. A Discrete Element Method based-approach for arched masonry structures under blast loads. *Eng Struct* 2020;216:110721.
- [6] Karmakar S, Shaw A. Response of RC plates under blast loading using FEM-SPH coupled method. *Eng Fail Anal* 2021;125:105409.
- [7] Sherburn JA, Roth MJ, Chen JS, Hillman M. Meshfree modeling of concrete slab perforation using a reproducing kernel particle impact and penetration formulation. *Int J Impact Eng* 2015;86:96–110.
- [8] Rabczuk T, Eibl J. Numerical analysis of prestressed concrete beams using a coupled element free Galerkin/finite element approach. *Int J Solids Struct* 2004;41(3–4):1061–80.
- [9] Lian YP, Zhang X, Zhou X, Ma ZT. A FEMP method and its application in modeling dynamic response of reinforced concrete subjected to impact loading. *Comput Methods Appl Mech Eng* 2011;200(17–20):1659–70.
- [10] Silling SA. Reformulation of elasticity theory for discontinuities and long-range forces. *J Mech Phys Solids* 2000;48(1):175–209.
- [11] Silling SA, Epton M, Weckner O, Xu J, Askari E. Peridynamic states and constitutive modeling. *J Elast* 2007;88(2):151–84.
- [12] Silling SA, Askari E. A meshfree method based on the peridynamic model of solid mechanics. *Comput Struct* 2005;83(17–18):1526–35.
- [13] Huang D, Lu G, Qiao P. An improved peridynamic approach for quasi-static elastic deformation and brittle fracture analysis. *Int J Mech Sci* 2015;94–95:111–22.
- [14] Wang Y, Zhou X, Wang Y, Shou Y. A 3-D conjugated bond-pair-based peridynamic formulation for initiation and propagation of cracks in brittle solids.

- Int J Solids Struct 2018;134:89–115.
- [15] Wu L, Huang D, Xu Y, Wang L. A rate-dependent dynamic damage model in peridynamics for concrete under impact loading. *Int J Damage Mech* 2020;29(7):1035–58.
- [16] Cheng Z, Zhang G, Wang Y, Bobaru F. A peridynamic model for dynamic fracture in functionally graded materials. *Compos Struct* 2015;133:529–46.
- [17] Lai X, Liu L, Li S, Zeleke M, Liu Q, Wang Z. A non-ordinary state-based peridynamics modeling of fractures in quasi-brittle materials. *Int J Impact Eng* 2018;111:130–46.
- [18] Wu L, Wang L, Huang D, Xu Y. An ordinary state-based peridynamic modeling for dynamic fracture of laminated glass under low-velocity impact. *Compos Struct* 2020;234:111722.
- [19] Wu L, Huang D, Bobaru F. A reformulated rate-dependent visco-elastic model for dynamic deformation and fracture of PMMA with peridynamics. *Int J Impact Eng* 2020;149:103791.
- [20] Silling SA, Askari A. Peridynamic model for fatigue cracking. Rep SAND2014-18590, Sandia Natl Lab 2014;
- [21] Ma X, Xu J, Liu L, Wang P, Feng Q, Xu J. A 2D peridynamic model for fatigue crack initiation of railheads. *Int J Fatigue* 2020;135(February):105536.
- [22] Jafarzadeh S, Chen Z, Bobaru F. Computational modeling of pitting corrosion. *Corros Rev* 2019;
- [23] Chen Z, Jafarzadeh S, Zhao J, Bobaru F. A coupled mechano-chemical peridynamic model for pit-to-crack transition in stress-corrosion cracking. *J Mech Phys Solids* 2021;146:104203.
- [24] Ni T, Pesavento F, Zaccariotto M, Galvanetto U, Zhu QZ, Schrefler BA. Hybrid

- FEM and peridynamic simulation of hydraulic fracture propagation in saturated porous media. *Comput Methods Appl Mech Eng* 2020;366:113101.
- [25] Bobaru F, Duangpanya M. A peridynamic formulation for transient heat conduction in bodies with evolving discontinuities. *J Comput Phys* 2012;231(7):2764–85.
- [26] Diana V, Carvelli V. An electromechanical micropolar peridynamic model. *Comput Methods Appl Mech Eng* 2020;365:112998.
- [27] Katiyar A, Agrawal S, Ouchi H, Seleson P, Foster JT, Sharma MM. A general peridynamics model for multiphase transport of non-Newtonian compressible fluids in porous media. *J Comput Phys* 2020;402:109075.
- [28] Guo L, Zhang X, Li W, Zhou X. Multi-scale peridynamic formulations for chloride diffusion in concrete. *Eng Anal Bound Elem* 2020;120:107–17.
- [29] Chen Z, Chu X. Numerical Fracture Analysis of Fiber - Reinforced Concrete by Using the Cosserat Peridynamic Model. *J Peridynamics Nonlocal Model* 2022;1–24.
- [30] Zhu F, Zhao J. Peridynamic modelling of blasting induced rock fractures. *J Mech Phys Solids* 2021;153:104469.
- [31] Diyaroglu C, Oterkus E, Madenci E, Rabczuk T, Siddiq A. Peridynamic modeling of composite laminates under explosive loading. *Compos Struct* 2016;144:14–23.
- [32] Zhang Y, Deng J, Deng H, Ke B. Peridynamics simulation of rock fracturing under liquid carbon dioxide blasting. *Int J Damage Mech* 2019;28(7):1038–52.
- [33] Wang Q, Wang Y, Zan Y, Lu W, Bai X, Guo J. Peridynamics simulation of the fragmentation of ice cover by blast loads of an underwater explosion. *J Mar Sci Technol* 2018;23(1):52–66.

- [34] Fan H, Bergel GL, Li S. A hybrid peridynamics-SPH simulation of soil fragmentation by blast loads of buried explosive. *Int J Impact Eng* 2016;87:14–27.
- [35] Fan H, Li S. A Peridynamics-SPH modeling and simulation of blast fragmentation of soil under buried explosive loads. *Comput Methods Appl Mech Eng* 2017;318:349–81.
- [36] Chen Z, Niazi S, Bobaru F. A peridynamic model for brittle damage and fracture in porous materials. *Int J Rock Mech Min Sci* 2019;122:104159.
- [37] Wu P, Zhao J, Chen Z, Bobaru F. Validation of a stochastically homogenized peridynamic model for quasi-static fracture in concrete. *Eng Fract Mech* 2020;237:107293.
- [38] Wu L, Huang D. Peridynamic modeling and simulations on concrete dynamic failure and penetration subjected to impact loadings. *Eng Fract Mech* 2022;259:108135.
- [39] Mitchell JA. A Nonlocal, Ordinary, State-Based Plasticity Model for Peridynamics. Rep SAND2011-4974C, Sandia Natl Lab 2011;1–34.
- [40] Lammi CJ, Vogler TJ. A nonlocal peridynamic plasticity model for the dynamic flow and fracture of concrete. Rep SAND2014-18257, Sandia Natl Lab 2014;
- [41] Jin L, Du X, Ma G. Macroscopic effective moduli and tensile strength of saturated concrete. *Cem Concr Res* 2012;42(12):1590–600.
- [42] Wu L, Huang D, Li Z, Yao X. Peridynamic modeling for impact failure of wet concrete considering the influence of saturation. *Int J Damage Mech* n.d.:1–37.
- [43] Zhao F, Wen H. Effect of free water content on the penetration of concrete. *Int J Impact Eng* 2018;121:180–90.
- [44] Vu XH, Malecot Y, Daudeville L, Buzaud E. Experimental analysis of concrete

- behavior under high confinement: Effect of the saturation ratio. *Int J Solids Struct* 2009;46(5):1105–20.
- [45] Malecot Y, Zingg L, Briffaut M, Baroth J. Influence of free water on concrete triaxial behavior: the effect of porosity. *Cem Concr Res* 2019;120:207–16.
- [46] Huang X, Kong X, Hu J, Zhang X, Zhang Z, Fang Q. The influence of free water content on ballistic performances of concrete targets. *Int J Impact Eng* 2020;139:103530.
- [47] Kumar V, Kartik K V, Iqbal MA. Experimental and numerical investigation of reinforced concrete slabs under blast loading. *Eng Struct* 2020;206:110125.
- [48] Li G, Zhao Y, Pang S, Li Y. Effective Young's modulus estimation of concrete. *Cem Concr Res* 1999;29(9):1455–62.
- [49] Vanadit-Ellis W, Davis LK. Physical modeling of concrete gravity dam vulnerability to explosions. 2010 Int. Waterside Secur. Conf. WSS 2010, n.d., p. 1–11.